

Using physics-based priors in a Bayesian algorithm to enhance infrasound source location

Omar Marcillo,¹ Stephen Arrowsmith,¹ Rod Whitaker,¹ Dale Anderson,¹
 Alexandra Nippres,² David N. Green² and Douglas Drob³

¹*Geophysics Group, Los Alamos National Laboratory, Los Alamos, NM 87545, USA. E-mail: omarcillo@lanl.gov*

²*AWE Blacknest, Brimpton, Reading, UK*

³*Space Science Division, US Naval Research Laboratory, Washington, DC 20375, USA*

Accepted 2013 September 2. Received 2013 August 29; in original form 2013 March 25

SUMMARY

We show improvements in the precision of the Bayesian infrasound source localization (BISL) method by incorporating semi-empirical model-based prior information. Given a set of backazimuths and delay times at ≥ 2 arrays, BISL scans a parameter space (that comprises the horizontal coordinates, celerity and origin time) for the most likely solution. A key element of BISL is its flexibility; the method allows the incorporation of prior information to constrain the parameters. Our research focuses on generating model-based propagation catalogues using a comprehensive set of atmospheric scenarios, extracting celerity distributions based on range and azimuth from the catalogues and using these distributions as prior probability density functions to enhance the location solution from BISL. To illustrate the improvements in source location precision, we compare the BISL results computed using uniform celerity distribution priors with those using enhanced priors; as applied to: (1) a set of events recorded across a regional network and (2) a large accidental chemical explosion recorded by six infrasound arrays in Eurasia. Finally, we discuss efforts to improve the numerical implementation of BISL by expanding the parameter space to cover a richer set of parameters that can include station-specific celerity distributions.

Key words: Probability distributions; Guided waves; Acoustic properties.

1 INTRODUCTION

Local, regional and global infrasound networks are used to detect, locate and characterize natural (e.g. volcanoes, lightning and storms) and manmade (e.g. mining blasts, chemical and nuclear explosions) sources of infrasound (Le Pichon *et al.* 2010). Various formalisms have been developed to use time of arrivals and backazimuths of infrasonic signals for event localization, for example inversion of time and backazimuth using linearized least squares (Ceranna *et al.* 2009), a wave front-curvature-based approach for locating near-field sources (Szuberla *et al.* 2009) and the Bayesian infrasonic source localization (BISL; Modrak *et al.* 2010). A key advantage of BISL is its flexibility; any probability distribution can be used as appropriate and prior constraints can be readily folded into the solution. This research aims to enhance the locations obtained by BISL by implementing semi-empirical model-based constraints in the algorithm in the form of prior probability density functions (PDFs) for celerity (used here instead of ‘group velocity’ to refer to the apparent horizontal velocity from source to receiver).

1.1 The BISL algorithm

The BISL algorithm estimates the most likely source location given a set of backazimuths and arrival times by performing a grid search over a 4-D parameter space (Modrak *et al.* 2010). This multidimensional parameter space includes the two horizontal coordinates (x_0 and y_0), celerity (v) and origin time (t_0). In the Bayesian framework, the posterior PDF $P(\mathbf{m}|\mathbf{d})$ assesses the probability of a model ($\mathbf{m} = \{x_0, y_0, v, t_0\}$) given a specific data set ($\mathbf{d} = \{t_i, \theta_i\}$) arrival times t_i and backazimuths θ_i) and is written as

$$P(\mathbf{m}|\mathbf{d}) = c(\mathbf{d})P(\mathbf{m})P(\mathbf{d}|\mathbf{m}), \quad (1)$$

where $P(\mathbf{m})$ is the prior PDF, $P(\mathbf{d}|\mathbf{m})$ the likelihood PDF and $c(\mathbf{d})$ a normalization function. $P(\mathbf{d}|\mathbf{m})$ is the joint distribution of the errors in backazimuth $\Theta(\theta_i|\mathbf{m})$ and origin time $\Phi(t_i|\mathbf{m})$ between the data and the forward model evaluated in each point of the parameter space (Modrak *et al.* 2010):

$$P(\mathbf{d}|\mathbf{m}) = \prod_i^n \Theta(\theta_i|\mathbf{m})\Phi(t_i|\mathbf{m}), \quad (2)$$

where n is the number of arrays in the network, $\Theta(\theta_i|\mathbf{m}) = \frac{1}{\sqrt{2\pi\sigma_\theta^2}} \exp[-\frac{1}{2}(\frac{\gamma_i}{\sigma_\theta})^2]$ and $\Phi(t_i|\mathbf{m}) = \frac{1}{\sqrt{2\pi\sigma_\phi^2}} \exp[-\frac{1}{2}(\frac{\varepsilon_i}{\sigma_\phi})^2]$ are the distributions of the differences between observed and predicted backazimuths and arrival times given by:

$$\gamma_i = \theta_i - \tilde{\theta}_i \text{ and } \varepsilon_i = t_i - \left(t_0 + \frac{d_i}{v}\right), \quad (3)$$

where $\tilde{\theta}_i$ and d_i the backazimuth and radial distance at station i , σ_θ and σ_ϕ the corresponding standard deviations. While these equations assume Gaussian statistics, they can be readily substituted by different probability distributions as appropriate. $P(\mathbf{m})$ accounts for any potential prior information that can be used to constrain the parameters. The prior distribution can be written as

$$P(\mathbf{m}) = p(x_0, y_0)p(t_0)p(v), \quad (4)$$

where $p(x_0, y_0)$, $p(t_0)$ and $p(v)$ are the prior PDFs for horizontal coordinates, origin time and celerity, respectively.

1.1.1 Marginalization

The posterior PDF (eq. 1) can be marginalized (integrated over specific dimensions) over any dimension of the parameter space. BISL marginalizes over the celerity (v), and origin time (t_0) to obtain a new posterior PDF over the probable event location $\{x_0, y_0\}$:

$$\begin{aligned} P(\{x_0, y_0\}|\mathbf{d}) &= \int_{\text{all } t_0, v} c(\mathbf{d})P(\mathbf{m})P(\mathbf{d}|\mathbf{m}) dt_0 dv \\ &= p(x_0, y_0) \int_{\text{all } t_0, v} c(\mathbf{d})p(t_0)p(v)P(\mathbf{d}|\{x_0, y_0, t_0, v\}) dt_0 dv \\ &= c'(\mathbf{d})p(x_0, y_0)P'(\mathbf{d}|\{x_0, y_0\}), \end{aligned} \quad (5)$$

where $c'(\mathbf{d})$ and $P'(\mathbf{d}|\{x_0, y_0\})$ are the new normalization function and likelihood PDF. The marginalization process allows the assimilation of prior information in the form of a prior PDF (eq. 4).

The earlier implementation of BISL (Modrak *et al.* 2010) uses basic priors that constrain lower and upper limits of celerity (0.22–0.35 km s⁻¹, respectively) and assigns uniform probabilities within this range. This range is selected to include the celerity of rays refracting in the thermosphere (0.22–0.28 km s⁻¹), stratosphere (0.28–0.31 km s⁻¹) and troposphere (0.30–0.35 km s⁻¹; modified from Cepelcha *et al.* 1998). The approach taken here is to create prior PDFs for celerity that assign different probabilities to subregions of the 0.20–0.35 km s⁻¹ interval. We defined these celerity subregions as: (1) 0.20–0.28 km s⁻¹ for thermospheric, (2) 0.28–0.31 km s⁻¹ for stratospheric and (3) 0.30–0.35 km s⁻¹ for tropospheric returns. By calculating celerity based on the historical archives of observed atmospheric conditions, that is the historical record of operational atmospheric data analysis and reanalysis products (e.g. NOAA GFS, NASA MERRA, ECMWF ERA40, etc.), we create propagation catalogues that are used to evaluate the distribution of the celerity for a specific range (r_a), azimuth (ϕ_a) and time (t_a) such that

$$p(v) = K(v, r_a, \phi_a, t_a), \quad (6)$$

where K is a function that retrieves and normalizes celerity distributions from the propagation catalogues such that $\int_{\text{all } v} K(v, r_a, \phi_a, t_a) dv = 1$. Assuming that there is no prior infor-

mation for the location and origin time of the event, we can write $p(x_0, y_0)p(t_0) = 1$. Eq. (4) can now be written as

$$P(\mathbf{m}) = p(v) = K(v, r_a, \phi_a, t_a). \quad (7)$$

Networks (groups of sensor arrays) can have complete or partial azimuthal coverage. Networks with arrays located at comparable distances and azimuths generally see similar atmospheric conditions, and therefore a unique prior PDF can be assigned to them. For example, Arrowsmith *et al.* (2013) described a large infrasonic event recorded by a regional network, where all arrays are located at very similar backazimuths (between 302° and 304°) and distances (between 7200 and 7500 km) from the ground truth; thus, a unique prior PDF can be assigned to all the elements of this network. On the other hand, networks with good azimuthal coverage may see very different atmospheric conditions depending on the highly anisotropic wind field; separate celerities and priors for each array would be ideal in this case. For example, Pichon *et al.* (2013) described another large infrasonic event recorded by multiple arrays of the global infrasound network (located at dissimilar distances and backazimuths); for this event different prior PDFs would better describe the propagation to different elements of the network. As the current implementation of BISL assumes a unique uniform celerity, we construct a general prior PDF by averaging the prior PDFs for each array of the network (based on the array's azimuth and range):

$$P(\mathbf{m}) = k \sum_{i=1}^n K_i(v, r_{a,i}, \phi_{a,i}, t_{a,i}), \quad (8)$$

where n is the number of arrays in the system, range ($r_{a,i}$), azimuth ($\phi_{a,i}$) and time ($t_{a,i}$) are specific for the i th array of the network, and $k = 1 / \int_{\text{all } v} (\sum_{i=1}^n K_i) dv$ is a new normalization coefficient.

2 MODEL-BASED PROPAGATION CATALOGUES

We generate propagation catalogues based on ray tracing using atmospheric specifications and extending the propagation to regional and global distances. Infrasound can propagate at local (few tens km), regional (hundreds km) and global distances (thousands km). At local distances, propagation is driven by the conditions of the troposphere; with topography and source geometry also playing a role in propagation (Arrowsmith *et al.* 2012). Returns from the troposphere, stratosphere and thermosphere, and signals in the geometric shadow zone can be recorded at regional distances (Kulichkov 2004). Returns from the stratosphere (after multiple bounces) are the main component of detection at global distances (Mutschlecner *et al.* 1999; Le Pichon *et al.* 2009).

At regional and global distances, propagation is determined by the local vertical structure of winds and adiabatic sound speed. To gauge the general morphology of infrasound propagation along a particular direction the effective sound speed approximation is often used. Using this approximation an infrasound duct will occur along a given direction of propagation when the ratio of the effective sound speed at the ground relative to aloft is less than 1, where the effective sound speed is defined as the adiabatic sound speed plus the projection of the wind along the direction of propagation. This approximation can break down for steep stratospheric arrivals, when the effective sound speed exceeds around 25 per cent the adiabatic sound speed, and for those thermosphere arrivals where the influences of attenuation invalidate the ray approximation. Another

limitation of the effective local sound speed approximation is that the atmospheric vertical structures can vary in range over mesoscale (10–200 km) and synoptic-scale (200–3500 km) distances; as well as temporally by hour, week and time of year; all to a varying degrees depending on the specific geographic region and time of year. In the context of this work describing the utilization of physics-based priors in the BISL algorithm the assumption of local effective sound speed is not unreasonable when acknowledging the above limitations.

2.1 Generating propagation catalogues

The atmosphere is a highly variable medium in space and time, and this influences acoustic wave propagation (Drob *et al.* 2003). A model-based propagation catalogue aiming to capture a comprehensive set of propagation features has to include atmospheric scenarios from a wide range of realizations (i.e. multiple years of atmospheric models). The generation of model-based propagation catalogues requires two elements: (1) a set of parameters that defines the conditions of the atmosphere and (2) a model for the propagation of sound in the atmosphere.

2.1.1 Atmospheric specifications

To account for the atmospheric variability, we use a hybrid multiyear ground-to-space (G2S) atmospheric data set that is based upon the National Ocean and Atmosphere Administration-Global Forecast System (NOAA-GFS; Kalnay *et al.* 1990; Han & Pan 2011) from the surface to 35 km, the National Aeronautics and Space Administration—Goddard Earth Observing System Model (NASA-GEOS5; Rienecker *et al.* 2008) from 35 to 75 km and the NRLMSISE-00 (Picone *et al.* 2002) and HWM07 (Drob *et al.* 2008) empirical climatology above 75 km. The multisource, spectral, hybrid-modelling approach used to produce the seamless 2-yr database of G2S atmospheric specifications is described in Drob *et al.* (2003). The G2S specifications maintain the $4\times$ daily synoptic-scale information content of the NOAA-GFS and NASA-GEOS5 atmospheric specifications to a resolution of $1^\circ \times 1^\circ$, while extending the fields into the thermosphere based on climatologies to the nearest hour to account for the dominant solar heating driven, migrating diurnal and semi-diurnal upper atmospheric tidal variations.

2.1.2 Ray tracing

We use pseudo range-dependent ray tracing to generate the propagation catalogues. Our implementation of the ray tracing uses the tau-p approximation (Garcés *et al.* 1998; Drob *et al.* 2010), and assumes range-independent propagation for each individual refraction. In this scheme, a ray that starts at the ground and is refracted (in the troposphere, stratosphere or thermosphere) uses the same atmospheric specification from the start to the bounce point. To continue the propagation, new atmospheric specifications are retrieved at each bounce point and used for the next bounce. To generate our propagation catalogues, rays are launched at azimuths covering 360° in steps of 30° , and elevation angles between 1° and 50° at 2° interval and extending out to 1000 and 10 000 km horizontal distances for regional and global catalogues, respectively. We selected 30° and 2° for the azimuth and elevation steps, respectively, to ensure acceptable coverage across all directions while maintaining an acceptable computational cost. We limit the propagation of the rays

to a maximum of 100 bounces; this arbitrary limit is set to constrain tropospheric returns that propagate unrealistically to global distances. Future work will explore enhancements to this approach and the creation of catalogues with higher spatiotemporal resolutions. We use geometrical propagation and absorption models along with our ray tracing model to estimate amplitude losses along the ray's propagation path.

2.1.3 Absorption and geometrical losses in ray propagation

Atmospheric absorption and geometrical attenuation are important factors for signal detection especially for long-range and high-altitude acoustic propagation. Our implementation of ray tracing does not explicitly account for the amplitude of the ray along the path; however, geometrical attenuation and absorption can be approximated in post-processing using the propagation history of each ray. Using the solutions for the eikonal and transport equations following Blom & Waxler (2012), we determine geometrical attenuation for the first bounce of the rays in the catalogue and propagate it for later bounces assuming the propagation is range independent. Assuming again range independence and using the Sutherland & Bass (2004) absorption model, we estimate the atmospheric absorption for the first bounce and propagate it for the subsequent bounces. Future research is planned with more sophisticated ray trace codes to explicitly account for and assess the overall significance of the effects of atmospheric range dependence as it relates to geometric spreading, as well as atmospheric absorption. Fee *et al.* (2010) noted that the Sutherland & Bass (2004) model overestimates the absorption especially in the upper atmosphere. For our absorption calculations we follow Waxler *et al.* (2012) by reducing the absorption in the thermosphere. We choose to correct the attenuation by a factor of 0.3. Figs 1(a)–(c) show examples of atmospheric profiles for temperature and pressure and the corresponding absorption (corrected for thermospheric altitudes) for two frequencies, 0.3 and 2 Hz. Temperature and pressure profiles were generated using G2S for date and time 2007-12-2 00:00:00 for 41.131°N and 112.896° , which corresponds to a detonation site of the Utah Test and Training Range (UTTR, see Hedlin *et al.* 2012). The absorption profiles show a continuous increase in absorption especially above the stratosphere-mesosphere interface (between 50 and 60 km). At an elevation of 120 km the absorption has increased roughly three orders of magnitude. These high values of absorption significantly attenuate the amplitude of rays refracted in the thermosphere and constrain the number and elevation of thermospheric bounces. To measure wave attenuation along the propagation path, we define the total loss (TL), measured in decibels, as

$$\text{TL} = -20 \log_{10} \frac{|p(r, z)|}{|p_0|}, \quad (9)$$

where $p(r, z)$ is the absolute value of the amplitude at range r and altitude z and p_0 the initial pressure. Figs 1(d) and (e) show our implementation of the ray tracing tau-p approximation using the profiles in panels (a) and (b) for various launch angles. The rays are colour coded with the respective values of TL. Note the dependency of frequency in the absorption; for the 2 Hz rays absorption above the stratosphere increases very rapidly.

By incorporating amplitude attenuation into the propagation catalogues in this way, we can estimate the rays that can be detected on the ground for specific scenarios: (1) frequency and amplitude of the source, (2) source–receiver geometry and (3) detection capabilities of the receiver. We start by defining the total loss threshold (TL_{TH}) as the maximum attenuation that a ray can suffer and still be

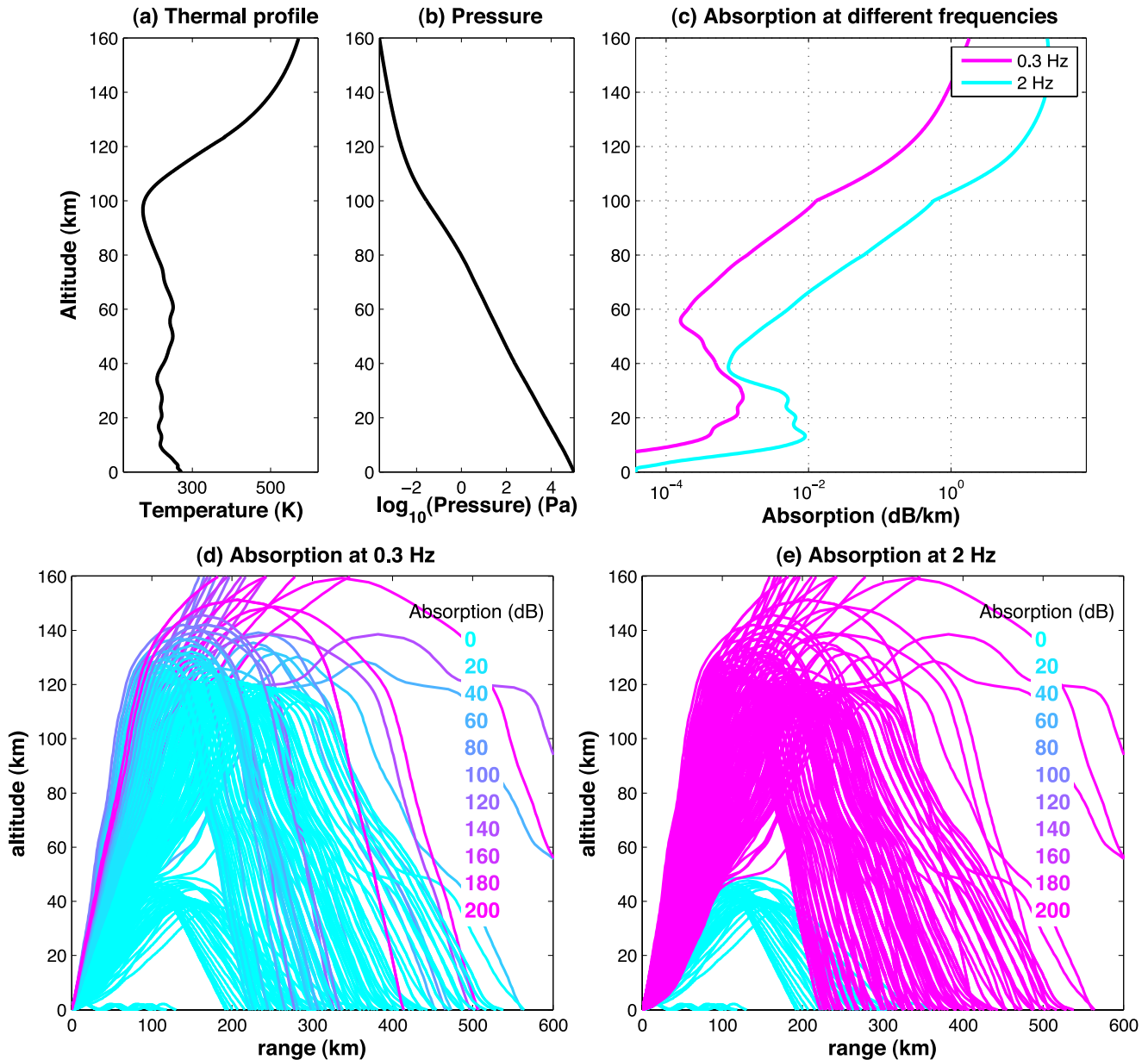


Figure 1. Ray tracing with atmospheric absorption for different frequencies. Panels (a) and (b) show an example of temperature and pressure profiles, respectively, used for the calculation of the atmospheric absorption profile in panel (c). Panels (d) and (e) show rays propagated through the profiles in (a) and (b). The rays are colour coded with the total absorption of the rays.

detected. Rays or sections of the rays with $TL > TL_{TH}$ are removed from the catalogues. For our catalogues, we assume a dominant signal frequency of 0.3 Hz and use $TL_{TH} = 112.5$ dB. This value is calculated using $p_0 = 8415$ Pa, which is the amplitude produced by 1 kt explosion and measured at 1 km from the source (Kinney & Graham 1985), and $p(r, z) = 0.02$ Pa, which is the amplitude of the atmospheric acoustic background noise (Bowman *et al.* 2005). In practice, a specific absorption catalogue may be selected based on the dominant frequency of the observed signals.

We generated two model-based propagation catalogues: (1) a regional catalogue, with the source of the rays located at 41.131°N and 112.896° , which corresponds to a detonation site of the UTTR (see Hedlin *et al.* 2012), and using G2S specifications from 2007 January 1 to 2008 December 31 and rays extending to ranges of 1000 km. (2) For the global catalogue, the ray tracing uses G2S

specifications also from 2007 January 1 to 2008 December 31, for locations within two latitudinally defined bands (30° to 60° and $\pm 30^\circ$) and rays extending to ranges of 10 000 km.

3 AZIMUTH DEPENDENT CELERITY-RANGE HISTOGRAMS

3.1 Extracting features from the propagation catalogues

From the model-based catalogues, we extract celerity and range for multiple bounces. To visualize these results, we introduce and use the celerity range histograms (CRHs), which display the ratio between the number of rays that reach the ground (hit) at specific ranges and celerities and the number of atmospheric specifications

used to generate the catalogue (profile). By using hit/profile to display the histograms CRHs generated using different time intervals and/or different number of atmospheric specifications can be easily compared. The CRHs use: (1) an evenly discretized range, from 0 to 1000 km and 0 to 5000 km for regional and global catalogues, respectively (we limit to 5000 km the maximum range to be displayed in the global CRHs to see the short-range features of the histograms), with 50 km interval and (2) evenly discretized celerities from 0.2 to 0.35 km s^{-1} with 0.01 km s^{-1} interval. As the propagation of acoustic energy is controlled by the highly anisotropic horizontal effective sound speed profiles, we developed azimuth dependent CRHs by grouping ray path features in four groups (quadrants) depending on launch azimuth. Quadrants covering $315^\circ\text{--}45^\circ$ (quadrant N) and $135^\circ\text{--}225^\circ$ (quadrant S) are used to capture the influence of meridional winds in propagation. The $45^\circ\text{--}135^\circ$ (quadrant E) and $225^\circ\text{--}315^\circ$ (quadrant W) quadrants are expected to capture the influence of zonal winds. In order to represent the temporal variability of the propagation, mainly related to changes in the stratospheric winds (Whitaker & Mutschlechner 2008), different CRHs were computed for different times of the year. Diurnal variability related to tides and its influence in thermospheric returns (Rind 1978; Garcés *et al.* 2002) are also not considered in this work for the sake of brevity but should also be considered in future work.

Fig. 2 shows two azimuth dependent CRHs for the regional catalogue; one for the winter months (defined here as January, February and March) and the other for the summer months (July, August and September). The main features in the histograms are rays with celerities corresponding to tropospheric, stratospheric and thermospheric returns. Tropospheric and stratospheric returns extend to the maximum range of the catalogue (1000 km), while the thermospheric returns are mainly constrained to the first bounce (between 200 and 600 km) due to high atmospheric absorption at high altitudes. Seasonal variability is noted for stratospheric returns at azimuths influenced by zonal winds, that is, the E quadrant shows more returns than the W quadrant for the winter months while more returns are present in the W quadrant compare to the E quadrant for the summer months. In addition, the seasonal changes in

tropospheric returns are associated with an eastward-directed acoustic duct that occurs during the winter months. In contrast, the thermospheric arrivals do not exhibit large seasonal variability as is to be expected due to lower seasonal changes in the thermospheric wind amplitudes.

Latitude specific CRHs for the winter months of the global catalogue are shown in Fig. 3 panels (a) and (b). To account for the dependence of latitude of the dominant zonal tropospheric and stratospheric wind jets, we separated the global histograms into latitude bands that represent mid (30° to 60°) and lower latitudes ($\pm 30^\circ$). Similar to the regional CRHs for the winter months (Fig. 2a), the seasonality of the stratospheric winds is also seen in the global catalogue; a higher density of stratospheric returns is seen for the mid latitudes at the E quadrant compare to the W quadrant (Fig. 3b). For lower latitudes (Fig. 3a), the W quadrant has a higher density of stratospheric returns compare to the other quadrants; similar behaviour is seen in the 4-yr cumulative summary of detections of the International Data Center described by Le Pichon *et al.* (2009). Thermospheric returns are constrained to the first 1000 km for both global CRHs. An outstanding feature in the mid-latitude CRHs (especially in the E quadrant) is the high density of returns with tropospheric celerities for ranges between 0 and around 2000 km (Fig. 3b). This tropospheric feature can be related to rays propagating over the ocean inside a low altitude waveguide (Che *et al.* 2011) and constrained to ranges less than 2000 km by our maximum number of allowed bounces (100).

3.2 Constructing celerity distributions from range slices of the CRH

The CRHs are used to generate PDFs for celerity. PDFs for celerity are constructed for specific source–receiver geometries in four steps: (1) determining the azimuth and radial distance between the source and receiver, (2) extracting the corresponding hit/profile distribution (vertical cross-sections of the CRH), (3) smoothing and (4) normalizing the distribution. Examples of steps (1)–(3) are shown in Fig. 4; panel b shows hit/profile distributions for the network

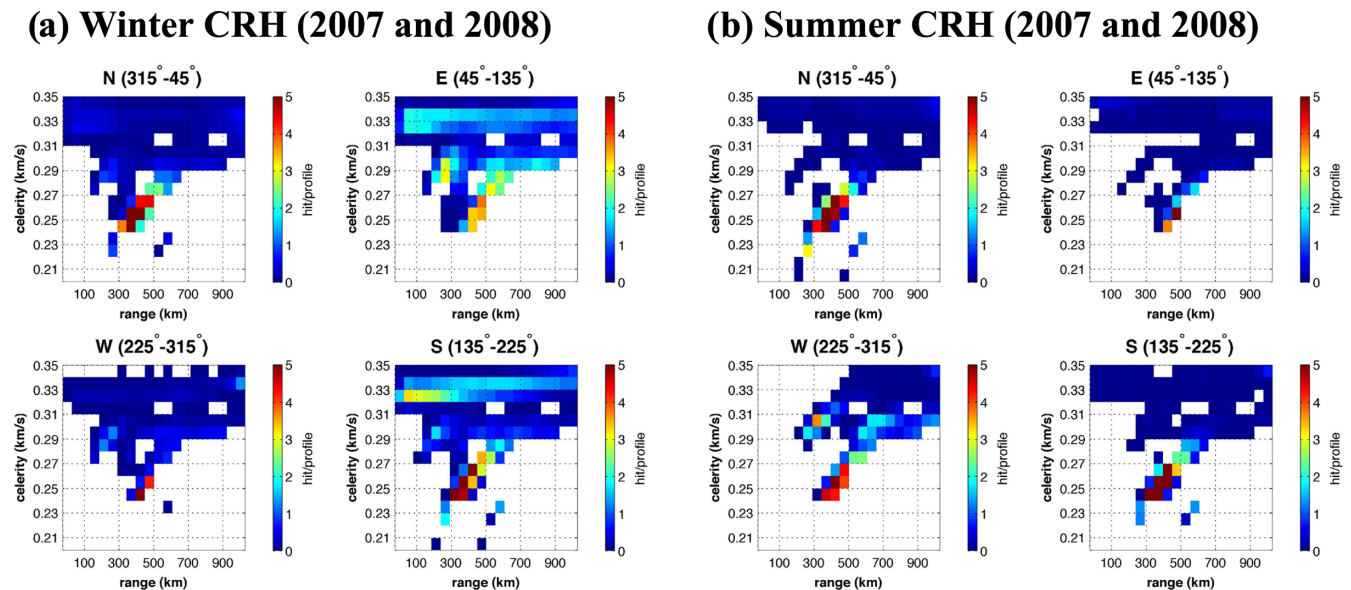


Figure 2. Seasonal (winter and summer) celerity range histograms (CRH) for years 2007 and 2008 for the Western US. CRHs display the ratio (colour axis) between the number of rays that return to ground (hit) and the associated number of profiles (used in the propagation modelling) at specific celerities (y-axis) and ranges (x-axis).

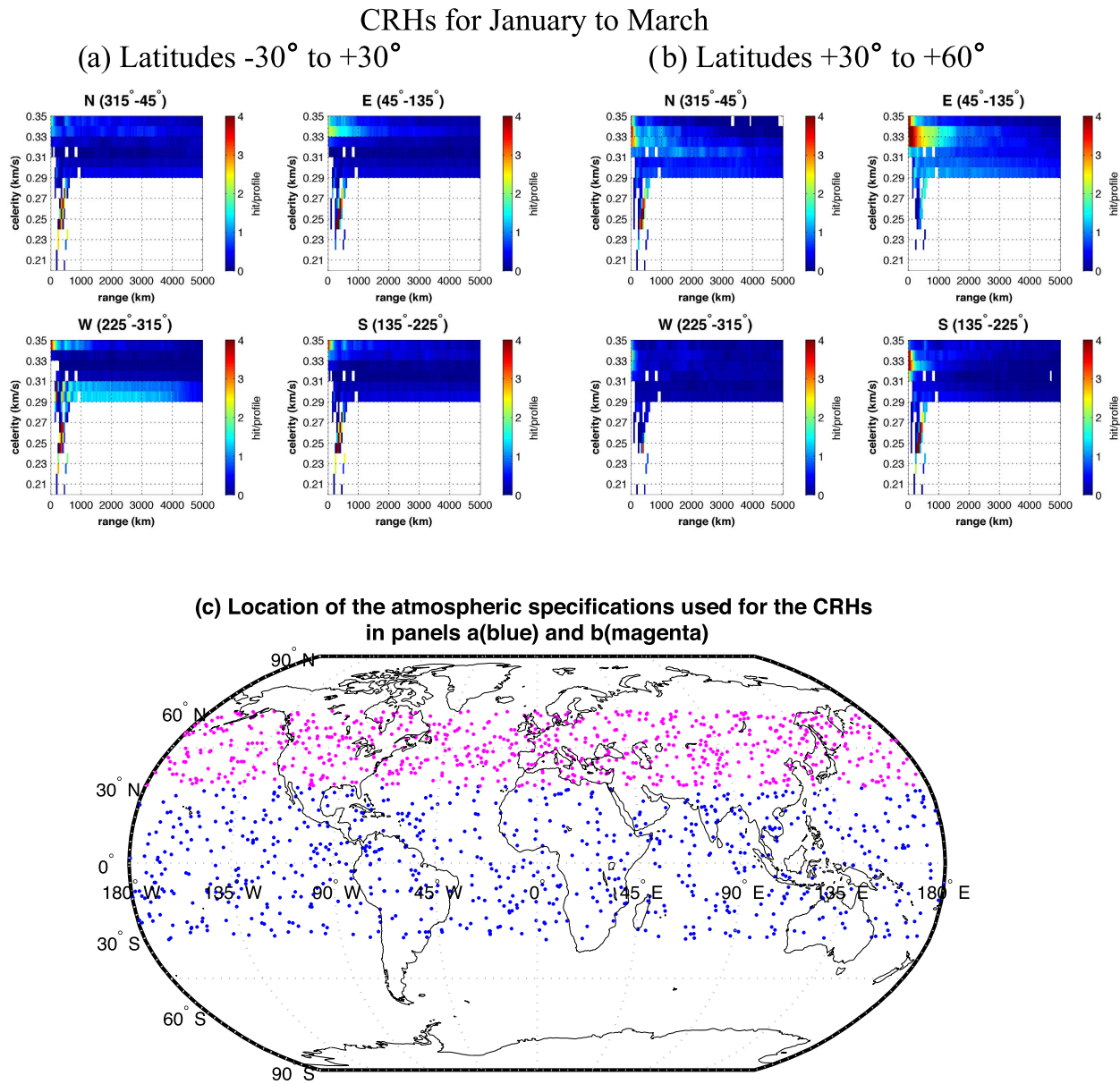


Figure 3. Global azimuth dependent CRH. CRHs for lower $\pm 30^\circ$ (a) and mid 30° – 60° (b) latitudes. (c) Map showing the random locations that are used to extract the atmospheric specifications used to build the winter CRHs in panels (a) (blue) and (b) (magenta).

configuration in panel a using winter and summer regional CRHs from Fig. 2. Forward and backward two-point moving averages are applied to smooth the distributions. The plots show significant differences in the distributions as a function of azimuth; for example for the winter months, station A shows very few returns with tropospheric celerities while B and C show higher numbers. Seasonality of the stratospheric winds between winter and summer and its influence in propagation can be seen between distributions at stations B and D.

4 USING A CRH-BASED PRIOR PDF TO ENHANCE BISL

Every point of the $\{x_0, y_0\}$ parameter subspace has CRH-based prior PDFs for each element of the network. Station-specific prior PDFs

are averaged into one network celerity distribution that is used to marginalize the celerity axis. We evaluated the performance of BISL with both uniform and CRH-based prior PDFs using infrasound signals from: (1) a set of regional events recorded by the University of Utah Seismic Network (UUS; Hale *et al.* 2010) and other stations in Nevada and (2) a large accidental chemical explosion recorded by six infrasound arrays in Eurasia.

4.1 Location of events at regional distances

Five events recorded by sensor arrays located in Utah and Nevada are used to compare the performance of the BISL method using uniform and CRH-based priors. We could find no publicly available ground-truth information for these events but the results suggest that the Hawthorne Army Ammunition Depot (HWAD) is the

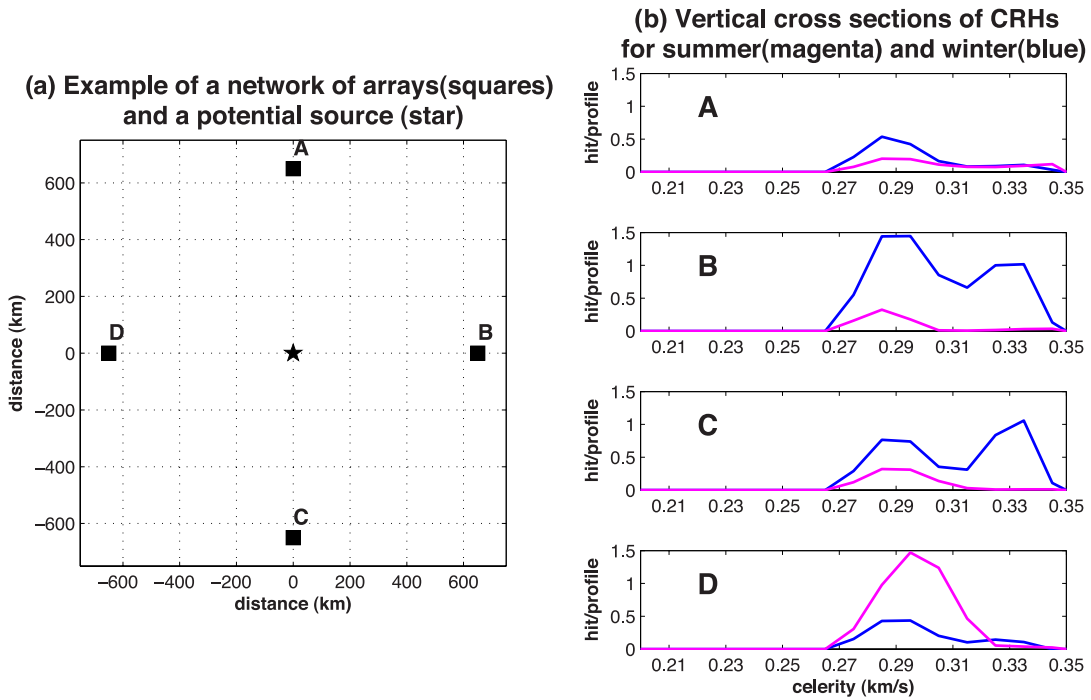


Figure 4. Example of CRHs' cross-sections at specific azimuths and ranges. (a) Distribution of a four-element network with arrays (squares) located at 650 km and different azimuths (0° , 90° , 180° and 270°) from a potential source (star). (b) Cross-sections of the Northern Hemisphere mid-latitude CRHs in Fig. 2 for the arrays and source in panel (a).

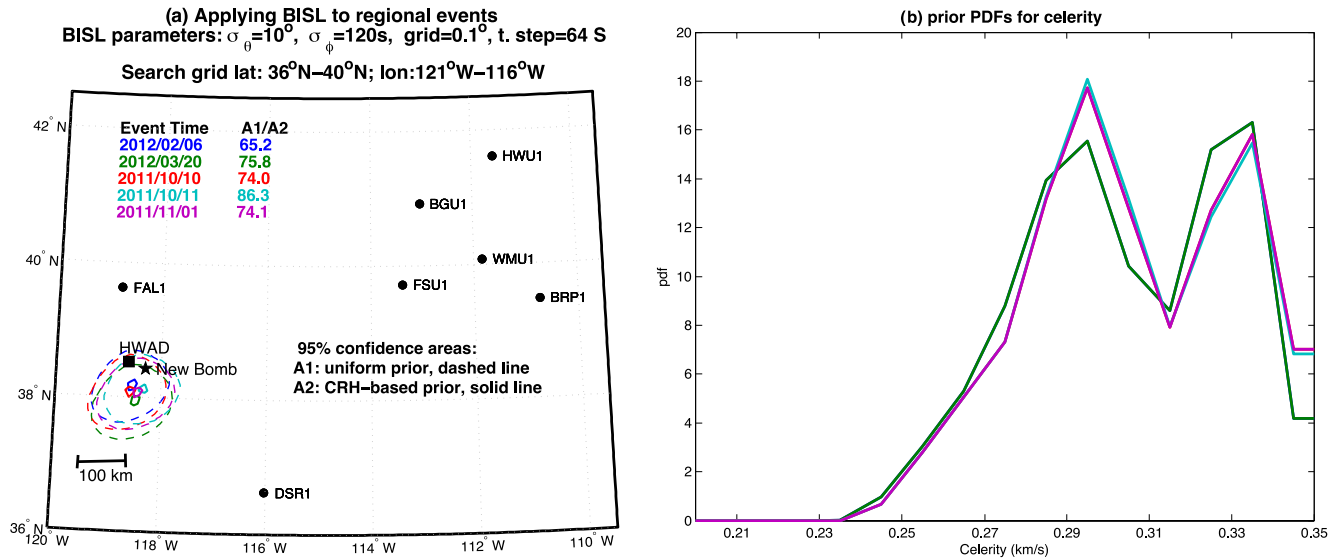


Figure 5. Using uniform and CRH-based prior PDFs for localization using BISL for events recorded at regional distances. (a) Location of the arrays in Utah and Nevada (black dots), 95 per cent confidence areas using uniform (dashed) and CRH-based (solid) priors, 'New Bomb' is one of the detonation sites [black star, (Negraru *et al.* 2010)] part of the Hawthorne Army Ammunition Depot (HWAD, black square). (b) CRH-based prior PDFs corresponding to the MAP points for each event localization. The PDFs for the 2012 February 06 (blue) and 2011 October 10 (red) events are similar to the 2012 March 20 (green) and 2011 November 01 (magenta) events, respectively.

potential source. For the location of these events, we discretized the parameter space in steps of 0.1° , 64 s and 0.01 km s^{-1} for the spatial, time and celerity axes, respectively, $\sigma_\theta = 10^\circ$ and $\sigma_\phi = 120 \text{ s}$. Arrowsmith *et al.* (2008) used $\sigma_\theta = 6^\circ$ and $\sigma_\phi = 40 \text{ s}$ for a study using similar arrays in Utah; we used a unique fixed value of $\sigma_\theta = 10^\circ$ for all the events to account for the different azimuthal deviations related to the different atmospheric conditions at different times

of the year. The large value of σ_ϕ was mainly chosen to account for the time step in the parameter grid (64 s). Fig. 5(a) shows the results of the application of BISL on five events that were detected across seven arrays. The 95 per cent confidence areas for uniform-prior solutions (dashed) and CRH-priors solutions (solid) show a significant reduction as a result of the use of physics base priors; ratios between uniform and CRH-based prior solution areas are

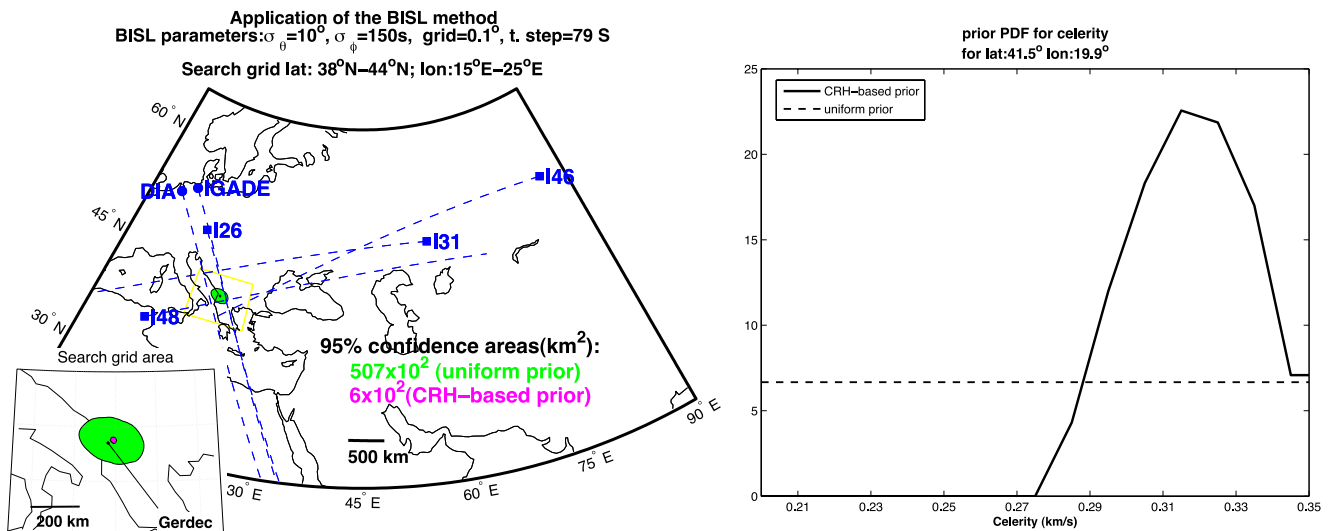


Figure 6. Using uniform and CRH-based prior PDFs for localization using BISL. (a) Location of the six stations (blue squares and dots) that recorded and identified the Gerdec explosion (black dot), 95 per cent confidence areas using uniform (green) and CRH-based (magenta) priors, perimeter of the BISL search grid shown in yellow. (b) Prior PDFs used for both uniform-prior-based and CRH-based BISL solutions.

around 70. Fig. 5(b) shows the CRH-based priors for each event configuration (source, receiver and time of the event) with the potential source located at the maximum *a posteriori* (MAP) point for each solution.

4.2 Location of events using long propagation event

As an example of the application of the CRH-based BISL for long-range propagation, we located an event from an accidental munitions dump explosion on 2008 March 15 (Green *et al.* 2011) in Gerdec, Albania. This event (black dot in Fig. 6a) was recorded by a total of six stations; four of the International Monitoring System (IMS) at distances of up to 4900 km (I26, I48, I31 and I46) and two operated by national facilities (DIA and IGADE). For the location of this event, we discretized the parameter space in steps of 0.1° , 79 s and 0.01 km s^{-1} for the spatial, time and celerity axes, respectively. As the step of the time axis (79 s) is higher here than the one for the events recorded at regional distances, we increased the value of the standard deviations in time to $\sigma_\phi = 150 \text{ s}$. Areas of green ($507 \text{ km} \times 10^2 \text{ km}$) and magenta ($6 \text{ km} \times 10^2 \text{ km}$) in Fig. 6(a) show the 95 per cent confidence areas for the location using uniform and CRH-based prior PDFs, respectively. These results show a significant enhancement in the localization precision (decrease in the 95 per cent confidence area). Using the MAP estimator, we found the most likely source location at 41.5°N and 19.9°E for both uniform-prior-based and CRH-based solutions, this source estimation is at 25 km radial distance and 65° azimuth from the ground truth [41.406°N and 19.632°E (Green *et al.* 2011)]. Further research is needed to assess the precision (95 per cent confidence area, measured in km^2) and also the accuracy (distance between ground-truth and estimated location, measured in kilometres) of this enhanced methodology using large numbers of ground-truth events.

5 DISCUSSION

The implementation of the CRH-based priors assigns higher probabilities of occurrence to more realistic scenarios based on numerical

modelling and increases the precision of the location algorithm. The ratios between solution areas using uniform and CRH-based priors show a significant increase in the precision for both regional and global events (see Figs 5 and 6). A statistical assessment of the enhancements in precision of this methodology requires a more comprehensive event catalogue. Multiyear event catalogues (e.g. mining explosions) where source information is available can provide an ideal platform to systematically assess the precision and accuracy of this methodology.

In the current implementation of BISL, one CRH-based prior PDF (averaged version of the array-specific celerity distributions) is assumed to represent the entire network. As the atmosphere is highly anisotropic, by averaging the stations-specific prior PDFs we are restricting the amount of prior information that can be provided to the algorithm. The current BISL implementation cannot accommodate station-specific prior information as it sees the network as a whole entity in the 4-D parameter space. To include station-specific priors in the methodology, the equations in the likelihood PDF (eq. 3) must change as

$$\varepsilon_i = t_i - \left(t_0 + \frac{d_i}{v_i} \right), \quad (10)$$

where v_i is now a vector of dimension equal to the number of arrival times–backazimuth pairs. Increasing the dimensions of the parameter space can dramatically increase the processing time of the marginalization process. We are exploring Monte Carlo integration as an alternative to integrate the expanded BISL posterior kernel to efficiently probe these more complex spaces (Mosegaard & Sambridge 2002) and enable real-time or near real-time applications.

Our current implementation of BISL also assumes that the measured backazimuth corresponds to the great circle receiver–source backazimuth. Drob *et al.* (2008) showed that for certain propagation directions, geographic regions and times of year the crosswinds can affect the direction of propagation and introduce significant offsets in the backazimuth estimation. The effects of cross wind and its influence in the measured backazimuth is assessed in BISL using a fixed value of σ_θ . Future work should explore

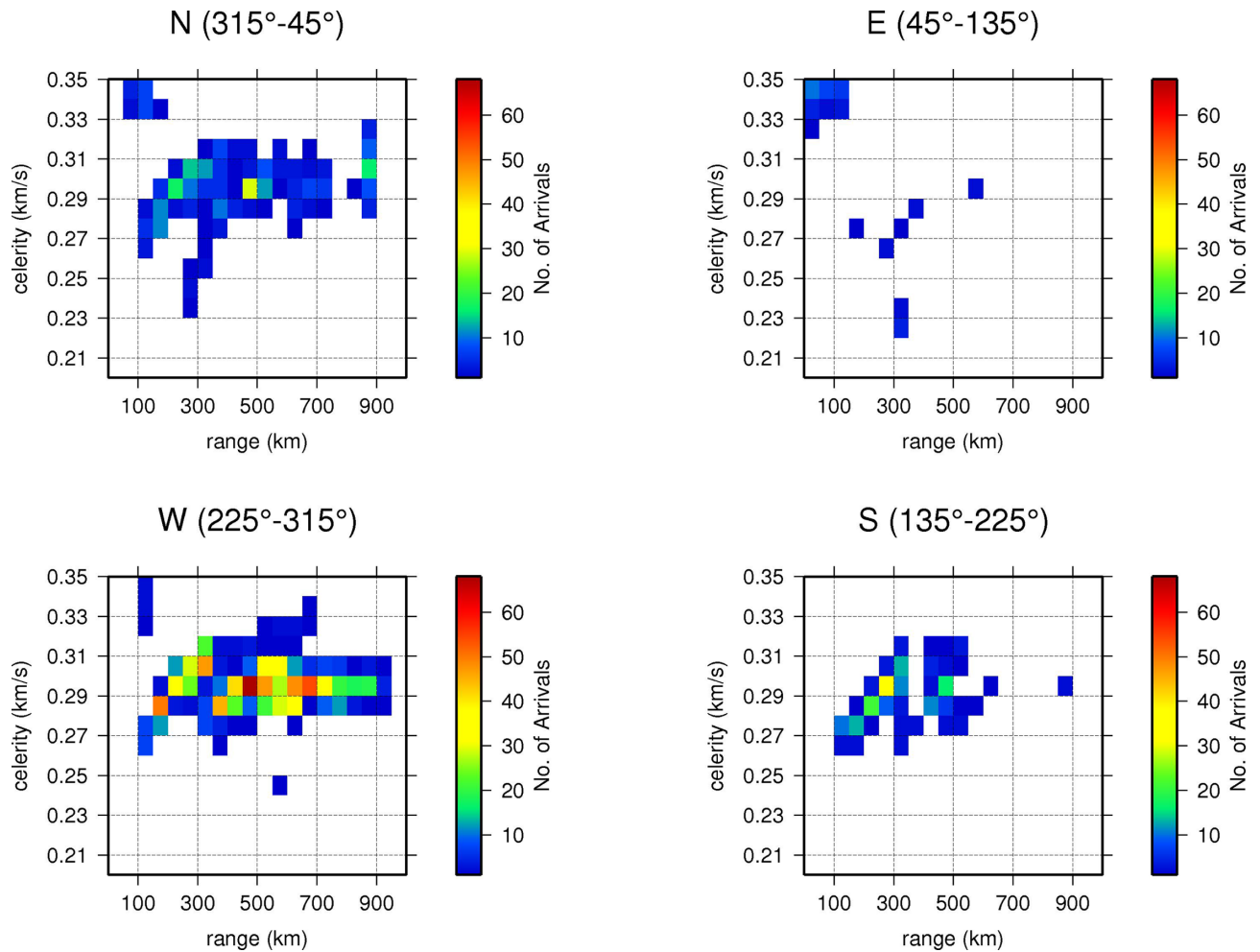


Figure 7. Azimuth dependent celerity range histograms for ground-truth event data for the western US during the summer months (July–September, inclusive), 2004–2008. All panels are shown on the same colour-scale, highlighting the predominant stratospheric propagation to the west during this period.

the use of the propagation catalogues to extract an azimuth-range dependent estimation of the expected errors in the determination of backazimuth and provide a network and season specific value for σ_{θ} .

The generation of event-based CRHs using ground-truth data can validate our model-driven approach for CRH generation. Fig. 7 shows an event-based CRH for the western US during the summer months (July–September inclusive), constructed using a combination of infrasound and seismic (air-to-ground coupled wave) recordings. The arrivals were generated by routine explosions at the UTTR, which have been catalogued in the RDSS database (<http://www.rdss.info>). The infrasound data are from 94 events between 2004 and 2008 and the seismic data are from the USArray (transportable array, network TA) for 39 events between 2006 and 2008. While the colour scale is the same for all four quadrants, the maximum number of picks per quadrant varies as follows: north—312, east—54, south—188 and west—990. The maximum peak-to-peak arrival at each station (both seismic and infrasound) is used to determine the traveltime and therefore the celerity (the methodology and results will be discussed fully in a future paper). The infrasound data show both thermospheric and stratospheric returns, whereas the seismic data show thermospheric, stratospheric and tropospheric. However, there was only one event where a clear thermospheric arrival was observed in the seismic data and this low

number of returns can be attributed to the higher attenuation of waves that probe higher sections of the atmosphere. This attenuation is particularly pronounced at frequencies above 1 Hz, where the signal-to-noise ratio for air-to-ground coupled waves is often highest. Future work is needed to investigate appropriate ways to combine propagation-based CRHs (useful because we can investigate large numbers of atmospheric realizations) with empirical CRHs (useful because these account for propagation effects not captured by the ray tracing modelling).

The significant increase in precision demonstrated here by incorporating prior information to the BISL method does not necessarily increase its accuracy (see Section 4.2, location of the Gerdec explosion using BISL), as the forward propagation model (which has corresponding error terms due to the limitations of the built-in *a priori* physical assumptions) does not change. The current implementation of BISL assumes azimuthally isotropic wave propagation. Deviations in the measured backazimuth and time of arrival resulting from the presence of wind are assessed by modifying σ_{θ} and σ_{ϕ} . Enhancing the accuracy of this methodology would require modifying the equation of propagation (eq. 3) to account for the anisotropy and heterogeneities of the atmosphere (especially for long-range propagation and events with high azimuthal coverage). Again, future work will investigate incorporating propagation models with different degrees of sophistication to find the optimal

balance between accounting for every aspect of the propagation phenomenology and practical computation efficiency.

6 CONCLUSIONS

Infrasound location techniques can make use of the detailed information available from current comprehensive, well-resolved historical databases of operational global atmospheric data analysis systems. These systems now extend well into the middle atmosphere. This paper has outlined a method for utilizing this information through the use of propagation-based catalogues that capture the salient anisotropic and spatiotemporally varying properties of infrasound propagation at least in the climatological average sense for a specific region or latitude. We show that implementing azimuth and range dependent prior information for celerity significantly enhances the precision of the BISL method, the ratios between solution areas using uniform and CRH-based priors are around 70 and 84 for regional and global event examples, respectively. This prior information is derived from the climatological averages of propagation calculations that utilize well-resolved specifications of the actual observed atmospheric conditions with $4\times$ daily (6-hourly) resolution to $1^\circ \times 1^\circ$ accuracy. Also, we introduced here the azimuth dependent CRHs as a tool to summarize and display propagation catalogues. Our ongoing research is focused now on studying further enhancements in the mathematical framework and application procedures to assimilate model- and event-based prior information in the BISL methodology.

ACKNOWLEDGEMENTS

We thank Leslie Casey for funding this work. This work was completed under the auspices of the U.S. Department of Energy by Los Alamos National Laboratory. DPD acknowledges support from Office of Naval Research. The GEOS-5 data utilized in conjunction with other data sources in the NRL G2S atmospheric specification for the two examples was provided by the Global Modeling and Assimilation Office (GMAO) at NASA Goddard Space Flight Center through the online data portal in the NASA Center for Climate Simulation. The NOAA GFS, also utilized in the G2S specifications, was obtained from NOAA's National Operational Model Archive and Distribution System (NOMADS), which is maintained at NOAA's National Climatic Data Center (NCDC). We would like to thank Junghyun Park and Brian Stump for providing us with the information for the events used in Section 4.1.

REFERENCES

- Arrowsmith, S.J. *et al.*, 2008. Regional monitoring of infrasound events using multiple arrays: application to Utah and Washington State, *Geophys. J. Int.*, **175**, 291–300.
- Arrowsmith, S.J., Whitaker, R.W., Maccarthy, J.K. & Anderson, D.N., 2012. A sources-of-error model for acoustic/infrasound yield estimation for above-ground single-point explosions, *InfraMatics*, **1**(1), 1–9.
- Arrowsmith, S.J., Marcillo, O. & Drob, D.P., 2013. A framework for estimating stratospheric wind speeds from unknown sources and application to the 2010 December 25 bolide, *J. geophys. Int.*, **195**(1), 491–503.
- Blom, P. & Waxler, R., 2012. Impulse propagation in the nocturnal boundary layer: Analysis of the geometric component, *J. acoust. Soc. Am.*, **131**(5), 3680–3690.
- Bowman, J.R., Baker, G.E. & Bahavar, M., 2005. Ambient infrasound noise, *Geophys. Res. Lett.*, **32**(9), 1–5.
- Cepelcha, Z., Borovička, J., Elford, W., ReVelle, D., Hawkes, R., Porubčan, V. & Šimek, M., 1998. Meteor phenomena and bodies, *Space Sci. Rev.*, **84**(3), 327–471.
- Ceranna, L., Le Pichon, A., Green, D.N. & Mialle, P., 2009. The Buncefield explosion: a benchmark for infrasound analysis across Central Europe, *J. geophys. Int.*, **177**(2), 491–508.
- Che, I.-Y., Stump, B.W. & Lee, H.-I., 2011. Experimental characterization of seasonal variations in infrasonic traveltimes on the Korean Peninsula with implications for infrasound event location, *J. geophys. Int.*, **185**(1), 190–200.
- Drob, D., Garcés, M., Hedlin, M. & Brachet, N., 2010. The temporal morphology of infrasound propagation, *Pure appl. Geophys.*, **167**(4), 437–453.
- Drob, D.P., Picone, J.M. & Garces, M., 2003. Global morphology of infrasound propagation, *J. geophys. Res.*, **108**(D21), 4680, doi:10.1029/2002JD003307.
- Drob, D.P. *et al.*, 2008. An empirical model of the Earth's horizontal wind fields: HWM07, *J. geophys. Res.*, **113**, A12304, doi:10.1029/2008JA013668.
- Fee, D., Steffke, A. & Garces, M., 2010. Characterization of the 2008 Kasatochi and Okmok eruptions using remote infrasound arrays, *J. geophys. Res.: Atmos.*, **115**(D2), 1–15.
- Garcés, M., Drob, D.P. & Picone, J.M., 2002. A theoretical study of the effect of geomagnetic fluctuations and solar tides on the propagation of infrasonic waves in the upper atmosphere, *J. geophys. Int.*, **148**(1), 77–87.
- Garcés, M.A., Hansen, R.A. & Lindquist, K.G., 1998. Traveltimes for infrasonic waves propagating in a stratified atmosphere, *J. geophys. Int.*, **135**(1), 255–263.
- Green, D.N., Vergoz, J., Gibson, R., Le Pichon, A. & Ceranna, L., 2011. Infrasound radiated by the Gerdec and Chelapechene explosions: propagation along unexpected paths, *J. geophys. Int.*, **185**(2), 890–910.
- Hale, J.M., Arrowsmith, S.J., Hayward, C., Burlacu, R., Pankow, K.L., Stump, B.W., Randall, G.E. & Taylor, S.R., 2010. Infrasound signal characteristics from small earthquakes, in *Proceedings of the 2010 Monitoring Research Review: Ground-Based Nuclear Explosion Monitoring Technologies*, Orlando, Florida.
- Han, J. & Pan, H.-L., 2011. Revision of convection and vertical diffusion schemes in the NCEP Global Forecast System, *Wea. Forecast.*, **26**(4), 520–533.
- Hedlin, M.A.H., de Groot-Hedlin, C. & Drob, D., 2012. A Study of infrasound propagation using dense seismic network recordings of surface explosions, *Bull. seism. Soc. Am.*, **102**(5), 1927–1937.
- Kalnay, E., Kanamitsu, M. & Baker, W.E., 1990. Global numerical weather prediction at the National Meteorological Center, *Bull. Am. Meteorol. Soc.*, **71**(10), 1410–1428.
- Kinney, G.F. & Graham, K.J., 1985. *Explosive Shocks in Air*, 2nd edn, Springer-Verlag, 282 pp.
- Kulichkov, S.N., 2004. Long-range propagation and scattering of low-frequency sound pulses in the middle atmosphere, *Meteorol. Atmos. Phys.*, **85**(1), 47–60.
- Le Pichon, A., Blanc, E. & Hauchecorne, A., 2010. *Infrasound Monitoring for Atmospheric Studies*, pp. 1–735, Springer-Verlag.
- Le Pichon, A., Vergoz, J., Blanc, E., Guilbert, J., Ceranna, L., Evers, L. & Brachet, N., 2009. Assessing the performance of the International Monitoring System's infrasound network: geographical coverage and temporal variabilities, *J. geophys. Res.*, **114**(D8), 1–15.
- Le Pichon, A., Ceranna, L., Pilger, C., Mialle, P., Brown, D., Herry, P. & Brachet, N., 2013. The 2013 Russian Fireball largest ever detected by CTBTO infrasound sensors, *Geophys. Res. Lett.*, **40**(14), 3732–3737.
- Modrak, R.T., Arrowsmith, S.J. & Anderson, D.N., 2010. A Bayesian framework for infrasound location, *J. geophys. Int.*, **181**(1), 399–405.
- Mosegaard, K. & Sambridge, M., 2002. Monte Carlo analysis of inverse problems, *Inverse Prob.*, **18**(3), R29–R54.
- Mutschleener, J.P., Whitaker, R.W. & Auer, L.H., 1999. An empirical study of infrasonic propagation, Report # LA-13620-MS. 1–69p. Sponsored by Los Alamos National Laboratory.
- Negraru, P.T., Golden, P. & Herrin, E.T., 2010. Infrasound propagation in the “Zone of Silence”. *Seismol. Res. Lett.*, **81**(4), 614–624.

- Picone, J.M., Hedin, A.E., Drob, D.P. & Aikin, A.C., 2002. NRLMSISE-00 empirical model of the atmosphere: statistical comparisons and scientific issues, *J. geophys. Res.*, **107**(A12), 1–16.
- Rienecker, M. *et al.*, 2008. The GEOS-5 data assimilation system: documentation of versions 5.0. 1, 5.1. 0, and 5.2. 0, NASA Tech. Memo, **104606**(27), 2008.
- Rind, D., 1978. Investigation of the lower thermosphere results of ten years of continuous observations with natural infrasound, *J. Atmos. Terrest. Phys.*, **40**(10–11), 1199–1209.
- Sutherland, L.C. & Bass, H.E., 2004. Atmospheric absorption in the atmosphere up to 160 km, *J. acoust. Soc. Am.*, **115**(3), 1012–1032.
- Szuberla, C.A.L., Olson, J.V. & Arnoult, K.M., 2009. Explosion localization via infrasound, *J. acoust. Soc. Am.*, **126**(5), EL112–EL116.
- Waxler, R., Lonzaga, J. & Assink, J., 2012. Non-linear infrasound signal distortion and yield estimation from stratospheric and thermospheric returns, in *Proceedings of the 2012 Monitoring Research Review: Ground-Based Nuclear Explosion Monitoring Technologies*, Albuquerque, New Mexico.
- Whitaker, R.W. & Mutschlecner, J.P., 2008. A comparison of infrasound signals refracted from stratospheric and thermospheric altitudes, *J. geophys. Res.*, **113**(D8), 1–13.